

A wide-field study of globular clusters in the nearest giant elliptical: Subaru/Suprime-Cam observations of Maffei 1[†]

Samuel Hinton^{1,2}, Ricardo Salinas³ Aaron J. Romanowsky^{4,5}, and maybe some others

¹Australian Astronomical Observatory, North Ryde, NSW 2113, Australia

²School of Mathematics and Physics, University of Queensland, QLD 4072, Australia

³Gemini Observatory

⁴Department of Physics & Astronomy, San José State University, San Jose, CA 95192, USA

⁵University of California Observatories, 1156 High Street, Santa Cruz, CA 95064, USA

Accepted ... Received ...; in original form ...

ABSTRACT

We have used imaging with the Subaru/Suprime-Cam search for and classify potential globular clusters in the nearby elliptical galaxy, Maffei 1. An area of $37' \times 31'$, centered on Maffei 1, was searched in the r' , i' and z' bands in sub-arcsecond seeing, allowing larger GCs to be partially resolved. Visually identified candidates found from PSF subtracted photometry and artificially generated sources were used to train machine learning algorithms to select candidate extended objects, and physical cuts on colour, ellipticity and size were used to reduce the candidates list. With these cuts, we report 288 “Class A” and 432 “Class B” globular cluster candidates for spectroscopic follow-up, where “Class A” candidates represent a higher level of confidence in the candidate. The found candidates range from 2pc to 15pc in size, and show reddening in excess of the reddening found in Galactic globular clusters.

Key words: Galaxies: individual: Maffei 1 – Galaxies: star clusters

1 INTRODUCTION

Add some general remarks on globular cluster systems.

Maffei 1 is a giant elliptical galaxy (Maffei 1968; Spinrad et al. 1971) located at only 0.5° North of the Galactic plane. This position implies large obscuration by dust from the Galactic disc which has hampered the measurement of even the most basic parameters of the galaxy.

Give main results from the literature

Its particular relative position has also conspired against the study of its globular clusters (GCs). Studies of its globular cluster system (GCS) have produced only a handful of GC candidates (Davidge 2002; Buta & McCall 2003; Davidge & van den Bergh 2005), whereas for its luminosity ($M_V \sim -20.80$, Fingerhut et al. 2007), the size of its GCS should be comparable to the one of Cen A, hosting ~ 1300 GCs (Harris 2010).

In this paper we present the first wide-field study of the Maffei 1 GCS system using Subaru/SuprimeCam imaging. In Sect. 2 we present the imaging data used, as well as its reduction and photometry. In Sect. 3 we present the GCs selection, together with the derived properties of the GCS. Sect. 4 puts our results on a wider context, while Sect. 5 summarizes the work and give conclusions.

2 SUBARU/SUPRIME-CAM OBSERVATIONS AND DATA REDUCTION

Maffei 1 images were obtained using Suprime-Cam (Miyazaki et al. 2002) located on the Subaru telescope, Mauna Kea, Hawaii. Suprime-Cam comprises 10 CCD detectors separated by $\sim 15''$ covering a field-of-view of $34' \times 27'$ with a pixel scale of $0.2''$. SDSS r' , i' and z' -band images were obtained during the night of January 5th, 2011. Several short exposures were taken with a $\sim 1'$ dither pattern, totalling 385, 280, and 280 seconds in the r' , i' and z' -bands, respectively.

Suprime-Cam images reduction was conducted within the SDFRED2 pipeline (Ouchi et al. 2004). Reduction steps include bias subtraction, flat-fielding, correction for atmospheric distortions, point spread function (psf) equalization (i.e. the normalization of the psf to a single shape across the detectors and exposures), sky subtraction, image alignment and finally, the combination of all exposures and detectors into single images. Final averaged images have a field-of-view of $\sim 37' \times 31'$ and a seeing quality of $0.72''$, $0.68''$ and $0.63''$, for r' , i' and z' , respectively. The field of view in z' is shown in Figure 1, and a detailed colour image of the galactic core is presented in Figure 2.

For the z' image set, which is used as the basis for the GC candidates identification given its higher image quality (see Sect. 3.1), a parallel alternative reduction process was adopted. The z' dataset not only provides the reddest band to pierce through the Galactic plane, but also contains the best seeing images. Even though the same SDFRED2 pipeline was mostly used, a couple of the afore-

[†] Based on data collected at Subaru Telescope, which is operated by the National Astronomical Observatory of Japan.

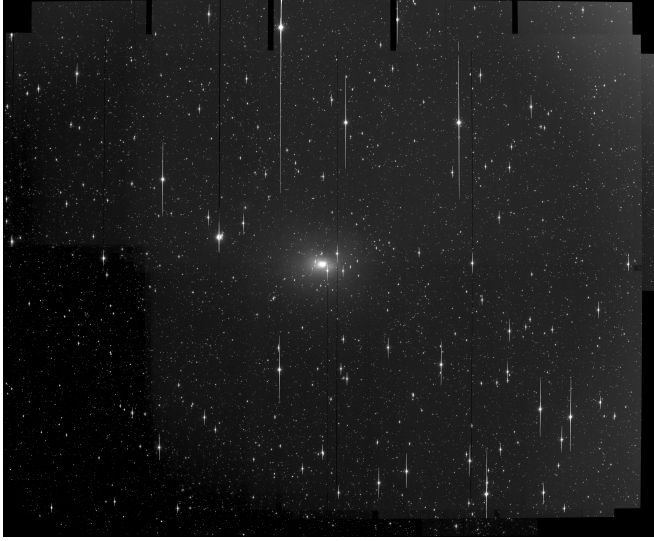


Figure 1. The Maffei 1 field as seen by Subaru-SuprimeCam in z' . Image size is approximately $37' \times 31'$. North is up and East is to the left.

mentioned reduction steps were skipped in order to maintain image manipulations that could alter the image quality to a minimum. Firstly, given the slight degradation of the psf towards the outer detectors, psf equalization across the chips would imply a loss of information on the best chips. For this reason the detectors were reduced independently and not combined into a single image as a final step. As a second difference, we did not apply any correction for atmospheric distortions, since it resulted in an increase of about 10% of the measured stellar full width at half maximum (fwhm) due to charge shifting to neighbor pixels. Finally, images with psf sizes significantly larger than the mean were excluded from the final image combination. This resulted in the rejection of zero to two exposures per chip.

Coordinate transformations and image combination for the individual detectors were carried out with DAOMASTER/MONTAGE2 (Stetson 1993, 1994), which give more flexibility than SDFRED2 for images with a small overlapping area. Measured fwhm on the combined z' images varies between $0.52''$ to $0.58''$ from detector to detector, which are noticeably better than the $0.62''$ measured on the combined full frame image given by SDFRED2.

As a last step prior to initial photometry, images presenting large background variations (containing Maffei 1 light or Galactic cirrus), were median filtered with an annulus kernel, with outer radius size of 150 pixel and an inner radius of 105 pixels; a large size that preserves point-like sources unaltered. Photometry and astrometry were performed on the images fully processed with the SDFRED2 pipeline.

2.1 Stellar photometry

Manual aperture and psf-fitting photometry were carried out on a chosen example tile using the stand-alone DAOPHOT2 photometric suite (Stetson 1987). The psf was modelled selecting ~ 120 – 140 bright and isolated stars on each detector. A quadratically varying Moffat function was found to provide the best description of the psf behaviour within the detectors.

Photometry for all the sources was also obtained using SExtractor (Bertin & Arnouts 1996), which additionally provides measurements of the size, orientation and ellipticity of the sources.

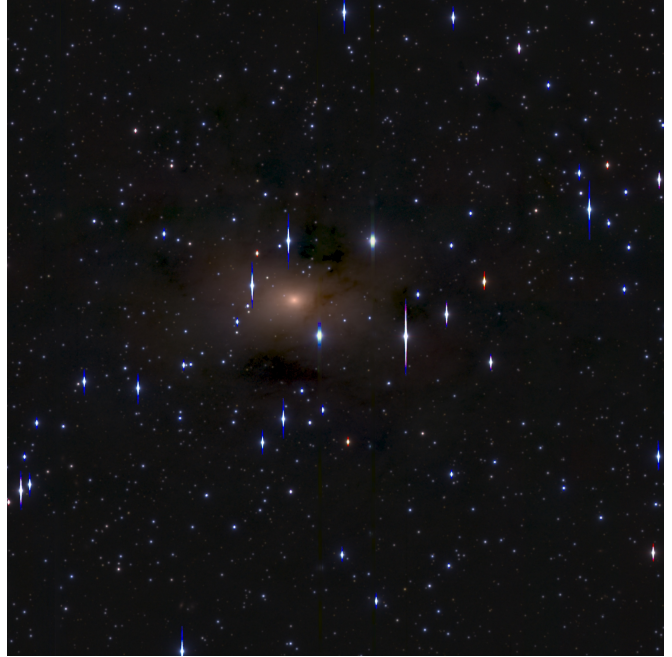


Figure 2. The core of Maffei 1 shown in z' , i' and r' , generated by STIFF (Bertin 2012). The image size is approximately $6.5' \times 6.5'$. North is up and East is to the left.

3 RESULTS

3.1 Selecting globular clusters candidates

The basic selection criterion for GCs in Maffei 1 rests on the non-stellar shape of their light profiles. This shape, usually smeared out for distant systems or in images with low spatial resolution, should be noticeable for the largest GCs in Maffei 1 given the galaxy's distance and the quality of the imaging. A similar approach has been applied successfully on ground-based imaging of GCs in the slightly more distant elliptical galaxy Centaurus A (Rejkuba 2001; Gómez et al. 2006; Gómez & Woodley 2007). As manual inspection of all sources was infeasible due to the number of sources, a machine learning approach was adopted in order to differentiate between stellar sources and extended sources. Initially, the neural network classifier contained inside SExtractor was utilised, but a posterior analysis has shown that clearly resolved sources have been assigned a `CLASS_STAR` parameter value as high as 0.98, which on a blind approach would have been classified as stars. Thus the algorithm was found to be insufficient, and a new algorithm was developed. Training of the machine learning algorithms was performed by combining artificially generated data and manual classification of SUPRIMECAM tiles.

Manual classification was performed by visual analysis of the star-subtracted z' -image of the CCD tiles produced by the psf-fitting algorithm in ALLSTAR. The images were visually inspected to look for residuals that revealed the presence of extended sources. The light profile of GCs (but also galaxies) would be over-subtracted in the central parts and under-subtracted in the wings, leaving an easily recognizable “ring-shaped” residual (see Fig. 3). A visual inspection of the residuals in a tile is a painstaking process, but provides benefit over only artificial data that does not model the full distribution of extended sources accurately.

Artificial stars and extended sources were added to the same visual inspection tiles by the use of the `mksynth` task in BAO-

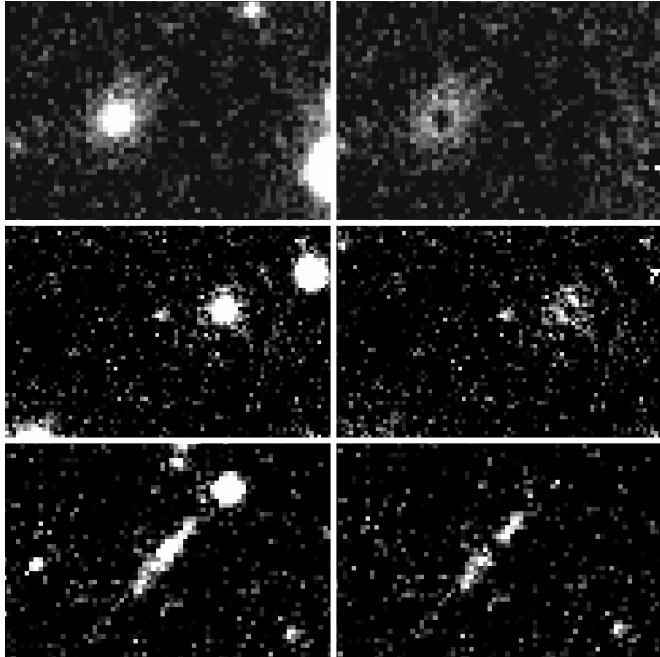


Figure 3. Three examples of the psf-subtraction technique applied on the final z images to reveal extended sources. The left panels show the original image, while the right panels are the psf-subtracted images. Top panels: A round object revealing a highly confident classification. Middle panels: A similar classification with a lower confidence due to the image noise. Bottom panels: An elongated extended object, in this case a galaxy viewed from the side, where the high ellipticity of the source allows differentiation between globular cluster and galaxy.

LAB (Larsen 1999). The psf input into the `mksynth` function was determined using by automatically selecting a number of candidate psf stars (based on flux criterion, star classification and source isolation), and generating a subsampled psf using the `digiphot` package in IRAF CITE. For the generation of artificial extended objects, the `mkcmpsf` task was used to generate a composite psf with a King model (King 1962) with concentration index of 30. The fwhm of the model was randomised to allow variation in the size of the artificial globular clusters. Both stars and extendeds were generated with uniform randomised magnitudes. The aritificial stars, uniformly distributed over the tiles, were added on top of the original data, to create an artifical tile ready for analysis. The analysis tiles were then background subtracted, and SExtractor used to detect source properties of both the artificial sources and manually classified sources. In total, over 30 000 artificial globular cluster candidates and 300 000 artificial stars were introduced over a series of 500 artificial images to create a large set of data. The weighting of the manually detected stars and extended objects from the original tile was increased to reflect their realism over artificial sources.

The input data was split into training, testing and validation sets, using ratios 0.4, 0.35 and 0.25 respectively, where multiple machine learning algorithms were trained on the training data, and the algorithm with the highest Matthews correlation coefficient(Matthews 1975) when evaluated on the validation set was selected as the final algorithm. The Matthews correlation coefficient was chosen to be maximised over other coefficients such as classifier accuracy, due to its fairness in dealing with unbalanced classes (Baldi et al. 2000; Jurman et al. 2012), which we expect to find with the number of point sources far exceeding the number of extended

sources. Expected performance of the algorithm was determined by fitting to the test data set, and the probability of correctly classifying an extended object as a function of half light radius and magnitude is shown in Figure 4.

The extended candidates for each tile given by the initial machine learning algorithm were then processed through the task `iShape`, a procedure in the BAOLAB software package, to gather more information on the candidates. This step is done seperately as computational constraints hinder the ability to run `iShape` on all detected sources, and so an initial candidate round must be selected. Information on χ^2 of the King fit, χ^2 of the delta model fit, and the fwhm of the King profile are added to the original data set. The manually selected candidates and artificially generated sources were also processed by `iShape`, and the improved dataset was used to train a second classifier in a similar fashion to the first, which was designed to remove many of the false positives from the initial classifier and improve accuray on only partially resolved globular cluster candidates. The probability of detecting a source as a globular cluster correctly, as a function of half light radius r_h and magnitude for the new classifier is shown in Figure 5. It important to note that the success rates shown in Figure 5 cannot be directly applied to the real data and thus only provide estaimtes due to the presence of additional selection cuts after attaining classification results. The matching accuracy on other tiles is expected to be lower due to artificial modelling not reflecting all the variations and subtleties of real global clusters and the lack of modelling other sources, such as compact dwarfs, stanard galaxies and other astronomical phenomenon outside stars and globular clusters.

Each candidate underwent aperture photometry on the fully reduced mosaics mentioned in Section 2, where colour magnitude corrections were performed by interpolating the dust maps from Schlegel et al. (1998) and applying the band extinction to redding ratios from Schlafly & Finkbeiner (2011). Magnitude calibration was performed by using the Landolt set of standard stars (Landolt 1992) that had been transformed via the equations given in Fukugita et al. (1996) into the SDSS system. Zero point magnitude calibrations were determined using the `fitparams` task in IRAF.

In order to reduce the number of false positives given by the second classifier and select only primary candidates, several important selection cuts were put in place. An absolute magnitude cut was implemented to remove sources brighter than $M_{z'} = -12$, and a $\chi^2_{\text{Delta}}/\chi^2_{\text{King30}} > 1$ cut removes objects better modelled as point sources. Objects with a King30 fwhm under 2pc (which corresponds to approximately half a pixel resolution of the object) or over 15pc, where distances calculated using the distance of Maffei 1 to be 2.7Mpc, were excluded from the sample. The maximal size cutoff was informed by the size distribution of known GCs presented in Harris et al. (2012). Objects with high ellipticity, such that $\epsilon > 0.25$ were removed in an effort to lower misidentified galaxies, also following the distributions presented in Harris et al. (2012). We present a more conservative cut than Harris et al. (2012), which would not select extended clusters and ultra-compact dwarfs in the size ranges of 20-30 pc (Evstigneeva et al. 2008; Huxor et al. 2005). Finally, a colour profile cut was introduced,to remove extended objects which have highly varying colour over their radial profile, to remove some of the galaxy's classified as globular clusters. The cut was calculated by determining the median deviation in the colour profile of the PSF stars, and removing all extended objects that varied by more than five times this value. These cuts reduced the original catalog of 1159 candidate objects output by the machine learning algorithm to 720 candidates.

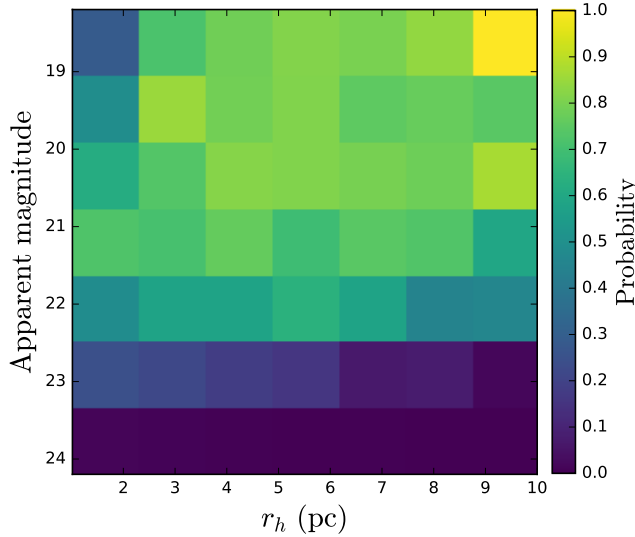


Figure 4. The probability $P(r_h, m_{z'})$ of correctly classifying an extended object using the initial classifier supplied with data from SExtractor. Classification accuracy decreases as r_h decreases, as the source becomes more pointlike. Similarly, we notice that objects dimmer than an apparent z' band magnitude of 16.5 are not classified correctly, as they are not detected by SExtractor. The high detection rates for this classifier come with a high number of false positives, with 31% of the classified extended objects being false positives. As apparent magnitude translates directly into electron count when generating artificial objects, the chance of detecting a dim source decreases with increasing r_h due to the peak brightness of the object falling.

The list of output candidates were further separated into two categories, referred to as Class A candidates and Class B candidates. Defining the ratio of matching strength between delta profiles and King profiles as $\chi_R^2 \equiv \chi_{\text{Delta}}^2 / \chi_{\text{King30}}^2$, candidates which have $\chi_R^2 > 1.5$ are categorized as Class A candidates, thus leaving Class B candidates with $1 \leq \chi_R^2 \leq 1.5$. Thus, Class A candidates represent objects that have a confident extended profile. The full catalog of 720 results is available in the online publication, and those utilising the data set may wish to apply their own additional cuts or selection criteria to suit their scientific purposes.

somewhere talk about no calibrations, difficulties getting standards, and lack of analogous control fields with which we can determine expected contamination

3.2 Globular clusters color-magnitude diagram

Comparing these colours to the colours of the globular clusters identified by CTIO instruments in Vanderbeke et al. (2014) shows a significant level of difference when taking all objects into account. The mean colours from Vanderbeke et al. (2014) are $\overline{r' - z'} = 0.44$, $\overline{r' - i'} = 0.29$ and $\overline{i' - z'} = 0.15$. In contrast, the mean colours for Class A candidates are $\overline{r' - z'} = 1.10$, $\overline{r' - i'} = 0.70$ and $\overline{i' - z'} = 0.40$, and the mean colours for Class B candidates are $\overline{r' - z'} = 1.26$, $\overline{r' - i'} = 0.80$ and $\overline{i' - z'} = 0.46$. The colours of the GC candidates are shown against their calculated absolute z' magnitude in Figure 6.

From the comparison, we see that the GC candidates for Maffei 1 are significantly redder than the GCs found in the Milky Way. The extra reddening of our GC candidates exceeds the reddening of 323 GCs found in the giant elliptical NGC5128 (Centau-

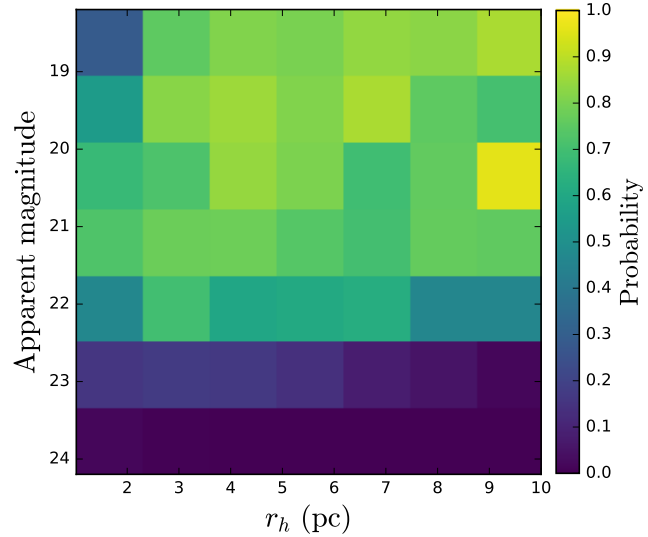


Figure 5. The probability $P(r_h, \mu)$ of correctly classifying an extended object using the secondary classifier, that is supplied with both data from SExtractor and data from ISHAPE fitting to a King profile. We notice similar difficulties in detecting the very faint and very compact sources as in the first classifier. The benefit of the additional information from ISHAPE is revealed when looking at the classification contamination: this classifier has a reduced false positive rate of 17%, and is removing more of the false positive stars without also removing extended sources.

rus A) by Sinnott et al. (2010), whose results give mean colours of $\overline{r' - z'} = 0.58$, $\overline{r' - i'} = 0.36$ and $\overline{i' - z'} = 0.22$.

This extra reddening was also found in the prior GC study of Maffei 1 by Buta & McCall (2003), who suggested that if the clusters are not obscured and variable extinction was not the primary source of reddening, that the difference could potentially be attributed to increase metallicity in Maffei 1 than the Milky Way. The candidates selected in this study reinforce the increased reddening of GCs in Maffei 1, and makes spectral analysis of metallicity a key science goal for future analyses.

The candidates' colours as a function of absolute magnitude in the z' band are shown in Figure 6. The colour distribution is shown in Figure 7. None of the distributions visually present strong signs of bimodality, however as prior studies in GCs have often shown bimodal distributions (Dirsch et al. 2003; Salinas et al. 2015), we analyse the bimodality rigorously using the Gaussian mixture modelling (GMM) implemented by Muratov & Gnedin (2010). Three main statistics are provided by GMM to distinguish between unimodal and bimodal distributions: a p -value representing the probability of attaining the same χ^2 from a unimodal distribution, the kurtosis of the distribution κ and the distance between the bimodal peaks $D \equiv |\mu_{\text{blue}} - \mu_{\text{red}}| / [(\sigma_{\text{blue}}^2 + \sigma_{\text{red}}^2) / 2]^{0.5}$. As with Salinas et al. (2015) and Usher et al. (2012), we utilise three necessary criterion for bimodality: $D > 2$, p -value < 0.1 and $\kappa < 0$. From this, we find no evidence of a bimodal distribution in the globular cluster candidates either for the Class A, Class B or total distributions. **BUT WHYYYY**

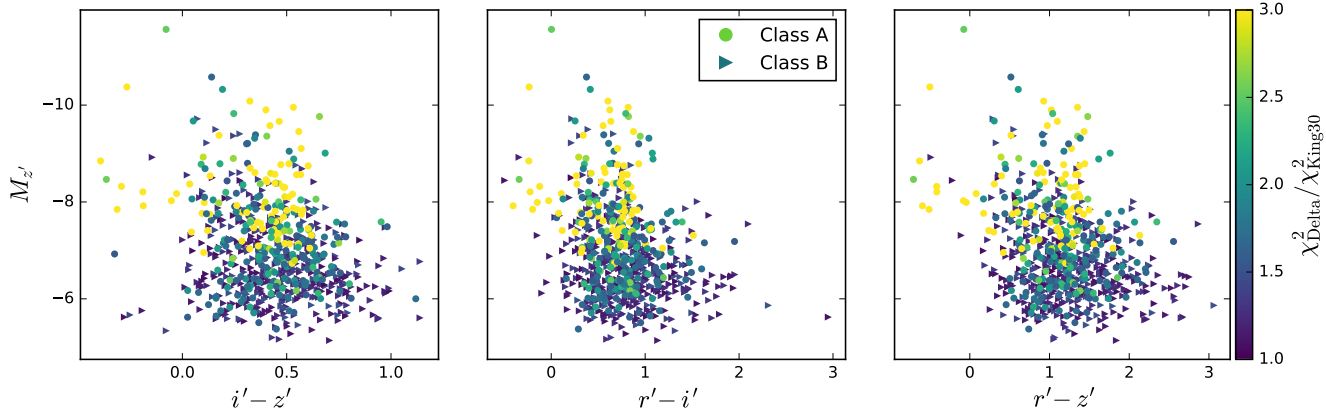


Figure 6. The determine colours of the GC candidates in the r' , i' and z' bands when applicable.

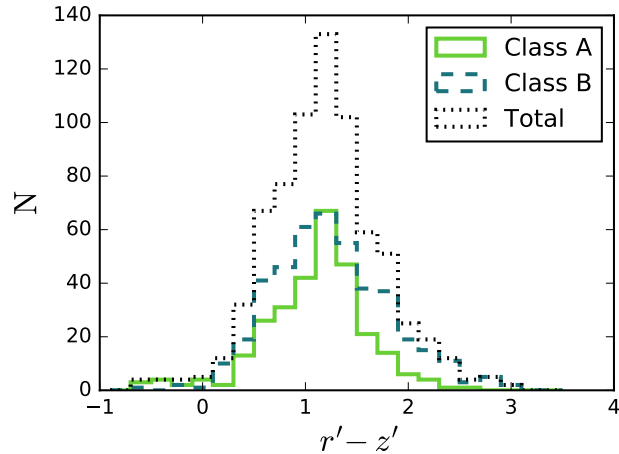


Figure 7. The colour distribution for all objects in total and when differentiated by class.

3.3 Globular cluster sizes

The differentiation between Class A and Class B objects gives rise to distinct differences in size distributions of the candidates. This distribution is shown in Figure 9, where we observe that Class A criteria preferentially select larger (and thus more extended) objects. Similarly, we observe that the brighter and more extended an object is, the higher the χ^2_R value gets (see Figure 8). As brighter objects correspond to a higher signal to noise above the background, this result is entirely expected. More interestingly are the number of Class B objects which have low χ^2_R values despite a large fitted King profile fwhm. These represent either objects with low signal to noise and poor fits to both delta and King models, potentially overlapping objects, or highly elliptical objects which, whilst being extended, do not fit the symmetric King profile well.

Talk about stuff in here. Ricardo, do you have a good citation for expected sizes of GCs? You said Harris?

*Lo*rem ipsum dolor sit amet, consectetur adipiscing elit. Ut purus elit, vestibulum ut, placerat ac, adipiscing vitae, felis. Curabitur dictum gravida mauris. Nam arcu libero, nonummy eget, consectetur id, vulputate a, magna. Donec vehicula augue eu neque. Pellentesque habitant morbi tristique senectus et netus et malesuada fames ac turpis egestas. Mauris ut leo. Cras viverra me-

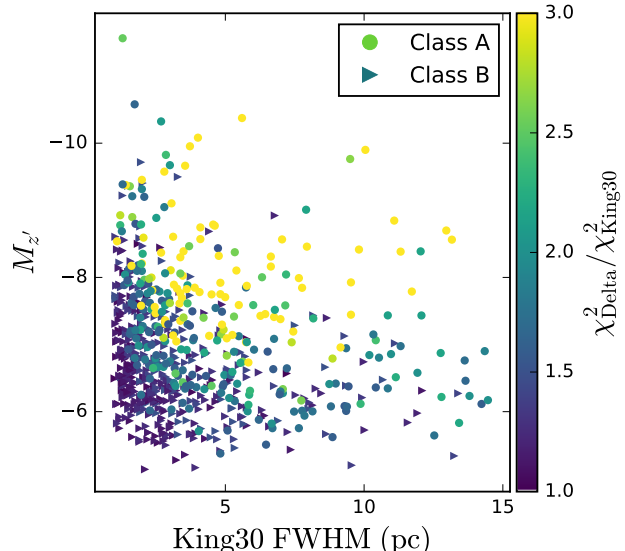


Figure 8. The fitted FWHM of a King30 profile for each GC candidate. Pixel values were transformed into parsecs using a galactic distance of 2.7 Mpc. Brighter and more extended objects have better fits to the King 30 profile than a delta profile, as expected.

tus rhoncus sem. Nulla et lectus vestibulum urna fringilla ultrices. Phasellus eu tellus sit amet tortor gravida placerat. Integer sapien est, iaculis in, pretium quis, viverra ac, nunc. Praesent eget sem vel leo ultrices bibendum. Aenean faucibus. Morbi dolor nulla, malesuada eu, pulvinar at, mollis ac, nulla. Curabitur auctor semper nulla. Donec varius orci eget risus. Duis nibh mi, congue eu, accumsan eleifend, sagittis quis, diam. Duis eget orci sit amet orci dignissim rutrum.

Nam dui ligula, fringilla a, euismod sodales, sollicitudin vel, wisi. Morbi auctor lorem non justo. Nam lacus libero, pretium at, lobortis vitae, ultricies et, tellus. Donec aliquet, tortor sed accumsan bibendum, erat ligula aliquet magna, vitae ornare odio metus a mi. Morbi ac orci et nisl hendrerit mollis. Suspendisse ut massa. Cras nec ante. Pellentesque a nulla. Cum sociis natoque penatibus et magnis dis parturient montes, nascetur ridiculus mus. Aliquam tincidunt urna. Nulla ullamcorper vestibulum turpis. Pellentesque cursus luctus mauris.

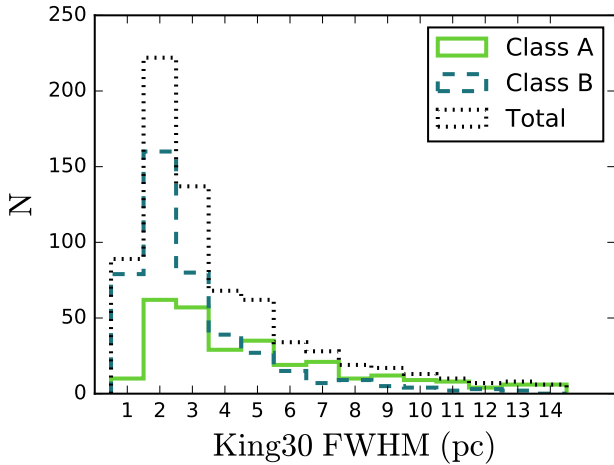


Figure 9. The size distribution of the FWHM fits of a King30 profile for both Class A and B candidates, using a distance to Maffei 1 of 2.7 Mpc. Class A candidates have a strong correlation with increased FWHM radius as expected.

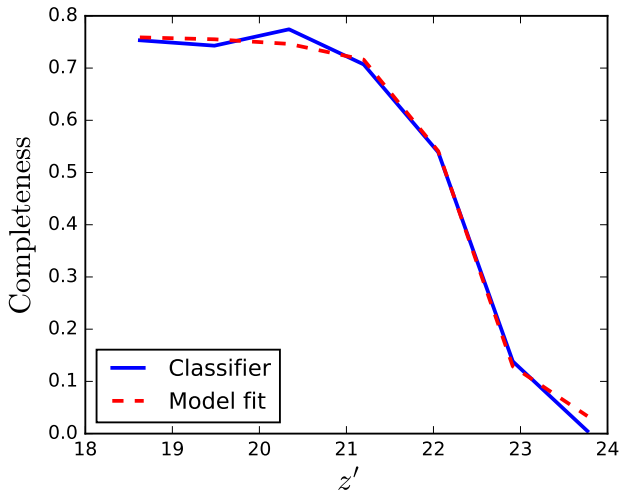


Figure 10. Completeness

4 DISCUSSION

To confirm that the globular cluster luminosity function (GCLF) we have found is reasonable, we wish to recover the true underlying distribution and compare against prior studies. We follow similar approach to Wehner et al. (2008); Alamo-Martínez et al. (2012); Salinas et al. (2015), where we model our detection completeness as

$$f = \beta \left(1 - \frac{\alpha(m - m_t)}{\sqrt{1 + \alpha^2(m - m_t)^2}} \right), \quad (1)$$

where β represents the maximal completeness, α the falloff rate and m_t the turnover magnitude.

We fit above function using our artificial data (see Figure 10), and correct our observed GCLF from the observed data by dividing by the completeness function, such that we get $d_{\text{underlying}} = d_{\text{observed}}/f$.

As with Salinas et al. (2015), we model the underlying distri-

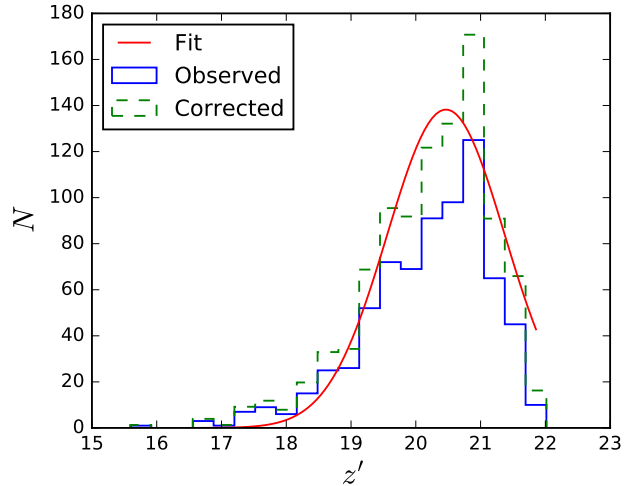


Figure 11. Completeness

bution as a Gaussian, and thus fit the underlying distribution with the model

$$d = \frac{a_0}{\sqrt{2\pi}\sigma_m} \exp \left[\frac{-(m - m_0)^2}{2\sigma_m^2} \right], \quad (2)$$

where a_0 is a scaling factor, σ_m is the dispersion, and m_0 is the mean magnitude. A fit to this model is shown in Figure 11, without output parameters $a_0 = 310 \pm 20$, $m_0 = 20.47 \pm 0.07$ and $\sigma_m = 0.91 \pm 0.07$.

The variable m_0 is itself given by $M_0 + \mu$, where M_0 is the absolute magnitude turnover and μ the distance modulus. Villegas et al. (2010) provides linear relationships between M_0 , $M_{z,\text{gal}}$ and μ , and σ_m , $M_{z,\text{gal}}$ and μ . $M_{z,\text{gal}}$ was given by transforming apparent magnitudes given in the B , V and I filters by Fingerhut et al. (2003) into the Sloan g and r filters by the transformation equations given by Jester et al. (2005). Apparent magnitude in g and r was then transformed to z using approximate colours $g - z$ and $r - z$ of a 10Gyr old metal-rich galaxy of $Z = 0.0115$ given by the interface CMD¹. Both colour transformations give $m_{z,\text{gal}} = 5.641$. $M_{z,\text{gal}}$ thus becomes a function of only μ . Utilise the relationships given in Villegas et al. (2010) and the recovered fit values to determine μ , finding $\mu \approx 29.1$ when using the M_0 relationship and $\mu \approx 26.0$ using the σ_m relationship. The naive mean of these values, $\mu \approx 27.5$ gives a distance of roughly 3.2 Mpc. Whilst the potential contamination and uncertainties in the Gaussian fit and relationships provided by Villegas et al. (2010) do not allow any reliable determination of distance, it does act as a useful consistency check that the determined globular cluster candidate catalog is not significantly different from expected population distribution.

5 SUMMARY AND CONCLUSIONS

Lore ipsum dolor sit amet, consectetuer adipiscing elit. Ut purus elit, vestibulum ut, placerat ac, adipiscing vitae, felis. Curabitur dictum gravida mauris. Nam arcu libero, nonummy eget, consectetuer id, vulputate a, magna. Donec vehicula augue eu neque. Pellentesque habitant morbi tristique senectus et netus et malesuada fames ac turpis egestas. Mauris ut leo. Cras viverra metus rhoncus

¹ http://stev.oapd.inaf.it/cgi-bin/cmd_2.7

sem. Nulla et lectus vestibulum urna fringilla ultrices. Phasellus eu tellus sit amet tortor gravida placerat. Integer sapien est, iaculis in, pretium quis, viverra ac, nunc. Praesent eget sem vel leo ultrices bibendum. Aenean faucibus. Morbi dolor nulla, malesuada eu, pulvinar at, mollis ac, nulla. Curabitur auctor semper nulla. Donec varius orci eget risus. Duis nibh mi, congue eu, accumsan eleifend, sagittis quis, diam. Duis eget orci sit amet orci dignissim rutrum.

Nam dui ligula, fringilla a, euismod sodales, sollicitudin vel, wisi. Morbi auctor lorem non justo. Nam lacus libero, pretium at, lobortis vitae, ultricies et, tellus. Donec aliquet, tortor sed accumsan bibendum, erat ligula aliquet magna, vitae ornare odio metus a mi. Morbi ac orci et nisl hendrerit mollis. Suspendisse ut massa. Cras nec ante. Pellentesque a nulla. Cum sociis natoque penatibus et magnis dis parturient montes, nascetur ridiculus mus. Aliquam tincidunt urna. Nulla ullamcorper vestibulum turpis. Pellentesque cursus luctus mauris.

ACKNOWLEDGMENTS

AJR was supported by National Science Foundation grants AST-0808099 and AST-0909237.

REFERENCES

- Alamo-Martínez K. A., West M. J., Blakeslee J. P., González-Lópezlira R. A., Jordán A., Gregg M., Côté P., Drinkwater M. J., van den Bergh S., 2012, *A&A*, 546, A15
- Baldi P., Brunak S., Chauvin Y., Andersen C. A. F., Nielsen H., 2000, *Bioinformatics*, 16, 412
- Bertin E., 2012, in Ballester P., Egret D., Lorente N. P. F., eds, *Astronomical Data Analysis Software and Systems XXI* Vol. 461 of *Astronomical Society of the Pacific Conference Series*, Displaying Digital Deep Sky Images. p. 263
- Bertin E., Arnouts S., 1996, *A&AS*, 117, 393
- Buta R., McCall M. L., 2003, *AJ*, 125, 1150
- Davidge T. J., 2002, *AJ*, 124, 2012
- Davidge T. J., van den Bergh S., 2005, *PASP*, 117, 589
- Dirsch B., Richtler T., Geisler D., Forte J. C., Bassino L. P., Gieren W. P., 2003, *AJ*, 125, 1908
- Evstigneeva E. A., Drinkwater M. J., Peng C. Y., Hilker M., De Propris R., Jones J. B., Phillipps S., Gregg M. D., Karick A. M., 2008, *AJ*, 136, 461
- Fingerhut R. L., Lee H., McCall M. L., Richer M. G., 2007, *ApJ*, 655, 814
- Fingerhut R. L., McCall M. L., De Robertis M., Kingsburgh R. L., Komljenovic M., Lee H., Buta R. J., 2003, *ApJ*, 587, 672
- Fukugita M., Ichikawa T., Gunn J. E., Doi M., Shimasaku K., Schneider D. P., 1996, *AJ*, 111, 1748
- Gómez M., Geisler D., Harris W. E., Richtler T., Harris G. L. H., Woodley K. A., 2006, *A&A*, 447, 877
- Gómez M., Woodley K. A., 2007, *ApJ*, 670, L105
- Harris G. L. H., 2010, *PASA*, 27, 475
- Harris G. L. H., Gómez M., Harris W. E., Johnston K., Kazemzadeh F., Kerzendorf W., Geisler D., Woodley K. A., 2012, *AJ*, 143, 84
- Huxor A. P., Tanvir N. R., Irwin M. J., Ibata R., Collett J. L., Ferguson A. M. N., Bridges T., Lewis G. F., 2005, *MNRAS*, 360, 1007
- Jester S., Schneider D. P., Richards G. T., Green R. F., Schmidt M., Hall P. B., Strauss M. A., Vanden Berk D. E., Stoughton C., Gunn J. E., Brinkmann J., Kent S. M., Smith J. A., Tucker D. L., Yanny B., 2005, *AJ*, 130, 873
- Jurman G., Riccadonna S., Furlanello C., 2012, *PLoS ONE*, 7, e41882
- King I., 1962, *AJ*, 67, 471
- Landolt A. U., 1992, *AJ*, 104, 340
- Larsen S. S., 1999, *A&AS*, 139, 393
- Maffei P., 1968, *PASP*, 80, 618
- Matthews B. W., 1975, *Biochimica et Biophysica Acta (BBA)-Protein Structure*, 405, 442
- Miyazaki S., Komiyama Y., Sekiguchi M., Okamura S., Doi M., Furusawa H., Hamabe M., Imi K., Kimura M., Nakata F., Okada N., Ouchi M., Shimasaku K., Yagi M., Yasuda N., 2002, *PASJ*, 54, 833
- Muratov A. L., Gnedin O. Y., 2010, *ApJ*, 718, 1266
- Ouchi M., Shimasaku K., Okamura S., Furusawa H., Kashikawa N., Ota K., Doi M., Hamabe M., Kimura M., Komiyama Y., Miyazaki M., Miyazaki S., Nakata F., Sekiguchi M., Yagi M., Yasuda N., 2004, *ApJ*, 611, 660
- Rejkuba M., 2001, *A&A*, 369, 812
- Salinas R., Alabi A., Richtler T., Lane R. R., 2015, *A&A*, 577, A59
- Schlafly E. F., Finkbeiner D. P., 2011, *ApJ*, 737, 103
- Schlegel D. J., Finkbeiner D. P., Davis M., 1998, *ApJ*, 500, 525
- Sinnott B., Hou A., Anderson R., Harris W. E., Woodley K. A., 2010, *AJ*, 140, 2101
- Spinrad H., Sargent W. L. W., Oke J. B., Neugebauer G., Landau R., King I. R., Gunn J. E., Garmire G., Dieter N. H., 1971, *ApJ*, 163, L25
- Stetson P. B., 1987, *PASP*, 99, 191
- Stetson P. B., 1993, in C. J. Butler & I. Elliott ed., *IAU Colloq. 136: Stellar Photometry - Current Techniques and Future Developments Further Progress in CCD Photometry*. p. 291
- Stetson P. B., 1994, *PASP*, 106, 250
- Usher C., Forbes D. A., Brodie J. P., Foster C., Spitler L. R., Arnold J. A., Romanowsky A. J., Strader J., Pota V., 2012, *MNRAS*, 426, 1475
- Vanderbeke J., West M. J., De Propris R., Peng E. W., Blakeslee J. P., Jordán A., Côté P., Gregg M., Ferrarese L., Takamiya M., Baes M., 2014, *MNRAS*, 437, 1725
- Villegas D., Jordán A., Peng E. W., Blakeslee J. P., Côté P., Ferrarese L., Kissler-Patig M., Mei S., Infante L., Tonry J. L., West M. J., 2010, *ApJ*, 717, 603
- Wehner E. M. H., Harris W. E., Whitmore B. C., Rothberg B., Woodley K. A., 2008, *ApJ*, 681, 1233

Table A1. Photometry of the first fifteen “Class A” (see main text for its definition) globular cluster candidates. Absolute magnitudes have been computed using $D = 2.7$ Mpc.

ID	RA	DEC	ϵ	$M_{z'}$	$m_{z'}$	$r' - z'$	King ₃₀ FWHM (pc)	King ₃₀ FWHM (px)
A1	2 ^h 38 ^m 21.5 ^s	59° 53' 55.56"	0.08	-8.144	19.013	0.773	1.5	0.53
A2	2 ^h 38 ^m 35.3 ^s	59° 53' 40.01"	0.14	-8.607	18.549	0.865	2.0	0.71
A3	2 ^h 38 ^m 8.8 ^s	59° 52' 28.73"	0.10	-7.504	19.653	1.459	4.9	1.69
A4	2 ^h 38 ^m 54.9 ^s	59° 52' 15.59"	0.22	-9.063	18.094	1.184	2.8	0.97
A5	2 ^h 38 ^m 12.9 ^s	59° 52' 0.17"	0.07	-8.581	18.575	1.349	7.0	2.44
A6	2 ^h 37 ^m 56.5 ^s	59° 51' 56.81"	0.25	-8.760	18.397	1.396	4.1	1.42
A7	2 ^h 38 ^m 36.7 ^s	59° 51' 36.32"	0.17	-7.319	19.838	0.991	3.6	1.26
A8	2 ^h 38 ^m 10.6 ^s	59° 50' 17.55"	0.20	-7.079	20.077	1.268	3.8	1.33
A9	2 ^h 38 ^m 10.8 ^s	59° 50' 0.74"	0.24	-8.177	18.980	1.399	6.6	2.30
A10	2 ^h 38 ^m 59.8 ^s	59° 49' 49.07"	0.24	-7.668	19.489	0.972	2.7	0.94
A11	2 ^h 38 ^m 37.2 ^s	59° 49' 40.83"	0.10	-7.140	20.017	1.499	5.5	1.90
A12	2 ^h 38 ^m 37.0 ^s	59° 49' 36.71"	0.16	-6.820	20.337	1.445	10.5	3.65
A13	2 ^h 38 ^m 27.5 ^s	59° 49' 23.25"	0.17	-8.399	18.757	1.102	11.3	3.92
A14	2 ^h 38 ^m 49.3 ^s	59° 48' 49.67"	0.11	-8.430	18.726	0.906	9.8	3.40
A15	2 ^h 38 ^m 43.5 ^s	59° 48' 17.19"	0.18	-7.167	19.990	1.400	4.8	1.68

Table A2. Photometry of the first fifteen “Class B” globular cluster candidates. Absolute magnitudes have been computed using $D = 2.7$ Mpc.

ID	RA	DEC	ϵ	$M_{z'}$	$m_{z'}$	$r' - z'$	King ₃₀ FWHM (pc)	King ₃₀ FWHM (px)
B1	2 ^h 38 ^m 21.8 ^s	59° 54' 6.40"	0.07	-9.381	17.776	0.528	1.5	0.52
B2	2 ^h 38 ^m 34.3 ^s	59° 53' 54.37"	0.14	-7.519	19.638	0.868	1.6	0.57
B3	2 ^h 38 ^m 24.5 ^s	59° 53' 54.88"	0.06	-8.432	18.725	1.383	1.1	0.38
B4	2 ^h 38 ^m 9.9 ^s	59° 53' 52.70"	0.18	-6.715	20.442	2.441	2.6	0.89
B5	2 ^h 38 ^m 18.8 ^s	59° 53' 43.42"	0.07	-6.751	20.406	1.510	1.7	0.60
B6	2 ^h 38 ^m 31.3 ^s	59° 53' 25.80"	0.22	-8.401	18.756	1.091	1.2	0.43
B7	2 ^h 38 ^m 32.6 ^s	59° 53' 24.71"	0.10	-7.242	19.915	1.124	1.3	0.45
B8	2 ^h 38 ^m 32.4 ^s	59° 53' 12.74"	0.12	-7.529	19.628	0.769	1.2	0.40
B9	2 ^h 38 ^m 38.0 ^s	59° 53' 9.44"	0.15	-6.993	20.164	1.419	1.8	0.61
B10	2 ^h 38 ^m 40.3 ^s	59° 52' 48.44"	0.08	-7.901	19.256	1.432	1.2	0.41
B11	2 ^h 38 ^m 6.6 ^s	59° 52' 38.96"	0.10	-6.040	21.117	0.975	6.3	2.19
B12	2 ^h 37 ^m 57.0 ^s	59° 52' 25.35"	0.19	-7.801	19.356	1.061	3.3	1.16
B13	2 ^h 38 ^m 52.6 ^s	59° 51' 58.44"	0.10	-7.572	19.584	1.411	1.6	0.54
B14	2 ^h 38 ^m 54.5 ^s	59° 51' 56.94"	0.18	-8.701	18.456	1.355	4.4	1.53
B15	2 ^h 38 ^m 47.3 ^s	59° 51' 39.85"	0.11	-7.868	19.288	0.562	1.2	0.43

APPENDIX A: GLOBULAR CLUSTER CANDIDATES PHOTOMETRY

Lorem ipsum dolor sit amet, consectetur adipiscing elit. Ut purus elit, vestibulum ut, placerat ac, adipiscing vitae, felis. Curabitur dictum gravida mauris. Nam arcu libero, nonummy eget, consectetur id, vulputate a, magna. Donec vehicula augue eu neque. Pellentesque habitant morbi tristique senectus et netus et malesuada fames ac turpis egestas. Mauris ut leo. Cras viverra metus rhoncus sem. Nulla et lectus vestibulum urna fringilla ultrices. Phasellus eu tellus sit amet tortor gravida placerat. Integer sapien est, iaculis in, pretium quis, viverra ac, nunc. Praesent eget sem vel leo ultrices bibendum. Aenean faucibus. Morbi dolor nulla, malesuada eu, pulvinar at, mollis ac, nulla. Curabitur auctor semper nulla. Donec varius orci eget risus. Duis nibh mi, congue eu, accumsan eleifend, sagittis quis, diam. Duis eget orci sit amet orci dignissim rutrum.